

Deposit Items

The Cr X-ray absorption *K*-edge structure of poorly crystalline Fe(III)-Cr(III)-oxyhydroxides

Jakob Frommer, Maarten Nachtegaal^{*}, Izabela Czekaj, Ruben Kretzschmar

^{*}E-mail: maarten.nachtegaal@psi.ch

3 Tables & 9 Figures

CONTENT

APPENDIX 1. PHASE CHARACTERIZATION	2
APPENDIX 2. SHELL-FITTING MODEL	3
APPENDIX 3. FOURIER TRANSFORMED EXAFS	9
APPENDIX 4. HIGH-ENERGY-RESOLUTION SPECTRA	10
APPENDIX 5. ADDITIONAL XANES SIMULATION	12
APPENDIX 6. SECOND DERIVATIVE SPECTRA	14
REFERENCES CITED	16

Appendix 1. Phase Characterization

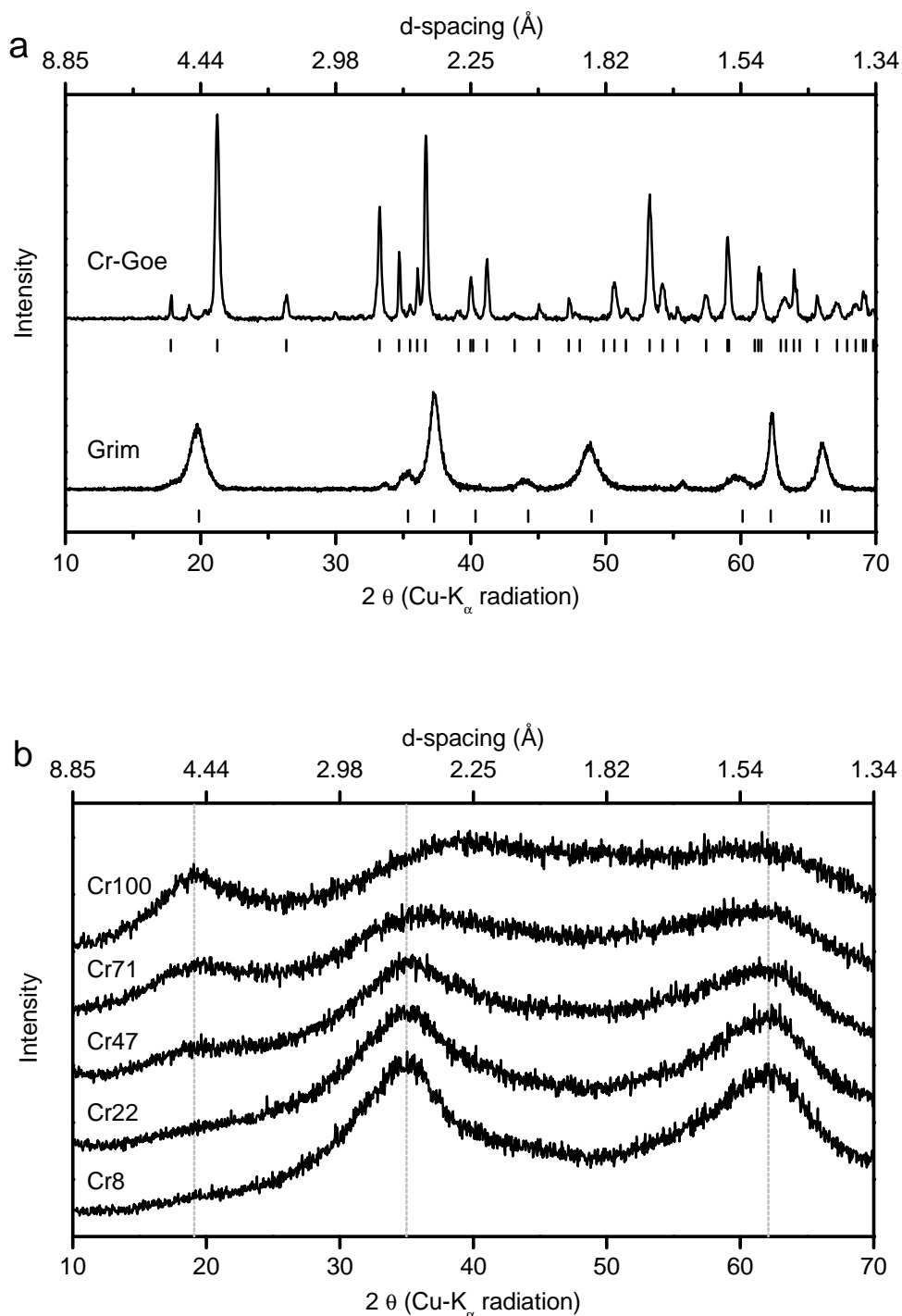


Figure S1: Powder X-ray diffraction patterns (a) of the crystalline reference phases and (b) of the series of Fe-Cr-oxyhydroxides. The small lines in panel a indicate the peak positions of the reference JCPDS pattern of goethite (PDF # 01-081-0464) and grimaldiite (PDF # 01-072-1207), respectively. The smoothed patterns of the series of Fe-Cr-oxyhydroxides are shown in Figure 1.

Appendix 2. Shell-fitting model

Parameterization of the multiple scattering paths

The MS paths within the central CrO_6 octahedra may significantly contribute to the Cr K -edge EXAFS signal in the R-range 2-4 Å (Boyanov et al., 2004). For their parameterization we slightly modified a recently described method for the parameterization of the MS paths in Fe-oxyhydroxides (Voegelin et al., 2010). The MS paths within an undistorted CrO_6 octahedron ($d(\text{Cr-O})=2\text{Å}$) up to a length of 4 Å were simulated with FEFF by using the potentials calculated from the Cr-goethite cluster (this allowed using the same S_0^2 and E_0 for both calculations). The lengths of the multiple scattering paths were defined relative to the (fitted) Cr-O distance. Assuming an uncorrelated atom displacement (Hudson et al., 1996) the DWPs for the multiple scattering paths were set as follows (DWP_O is the fitted O-shell DWP):

Triangular paths:	$\text{DWP}_{\text{MS}} = \text{DWP}_{\text{O}}$
Collinear 3-leg-paths:	$\text{DWP}_{\text{MS}} = 2 * \text{DWP}_{\text{O}}$
4-leg-paths involving 2 different neighboring atoms:	$\text{DWP}_{\text{MS}} = 2 * \text{DWP}_{\text{O}}$
4-leg-paths involving 1 neighboring atom only:	$\text{DWP}_{\text{MS}} = 4 * \text{DWP}_{\text{O}}$.

Figure S2 shows the sum of the MS paths of the best-shell fit to the Cr8 EXAFS (cf. Table 1) as an example. The amplitude of the MS paths is comparable to the one of the signal in the R-range 3-3.5 Å.

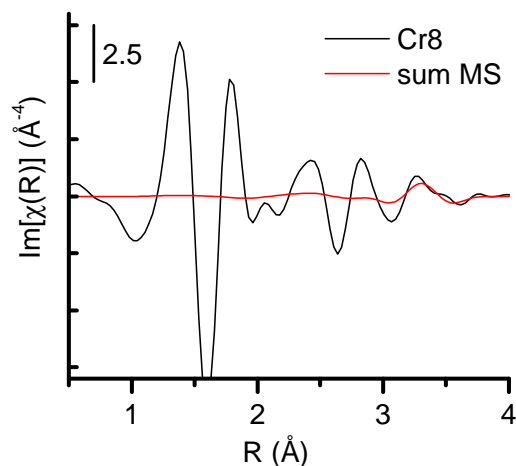


Figure S2: Imaginary part of the Fourier transformed sum of the MS paths within the CrO_6 octahedron. The imaginary part of the Fourier transformed Cr8 is shown for comparison.

Exchange correlation potential for the atomic background

The computation of the theoretical EXAFS standards (i.e., phase and amplitude functions) involves the determination of the fine structure and the atomic background. For both calculations an exchange correlation potential needs to be specified. By default FEFF uses the Hedin-Lundqvist exchange correlation potential for the computation of the fine structure (ixc-index) in both, the XANES and EXAFS part. For the determination of the atomic background (ixc0-index) the use of the Hedin-Lundqvist potential is recommended for the EXAFS part, whereas the ground state potential is recommended for the XANES part. Shell-fits of the first shell (R : 1-2 Å) by using theoretical standards calculated with the default settings (ixc0=0, i.e., Hedin-Lundqvist for the atomic background) deviated from the data mainly in the R -range 1.5-2 Å (Fourier transformed EXAFS; Figure S3a). This misfit could be reduced by using theoretical standards calculated with the ground-state potential for the atomic background (ixc0=2). The fits are shown in Figure S3a and the corresponding fit parameters are summarized in Table S1. The use of the ground state potential (for the atomic background) resulted in a larger fitted DWF and a larger fitted S_0^2 in comparison to the Hedin-Lundqvist potential. Figure S3b shows the computed Cr-O single scattering paths for both theoretical calculations. Using the ground state potential for the calculation of the atomic

background results in a reduced amplitude at lower k -values ($k < 7 \text{ \AA}^{-1}$), whereas the amplitude at higher k values is hardly affected. The results of the shell-fits of the Cr-O shell indicate that the Cr-O single scattering path calculated with $\text{ixc0}=2$ seem to provide a better fit to the experimental data (Table S1). The reason for the improvement is currently not clear. However, we obtained similar results for Cr K -edge EXAFS spectra measured at three different beamlines (SuperXAS, DUBBLE, HASYLAB A1) and for different settings of the AUTOBK algorithm, such that artifacts related to experimental noise and to the background subtraction procedure can be excluded.

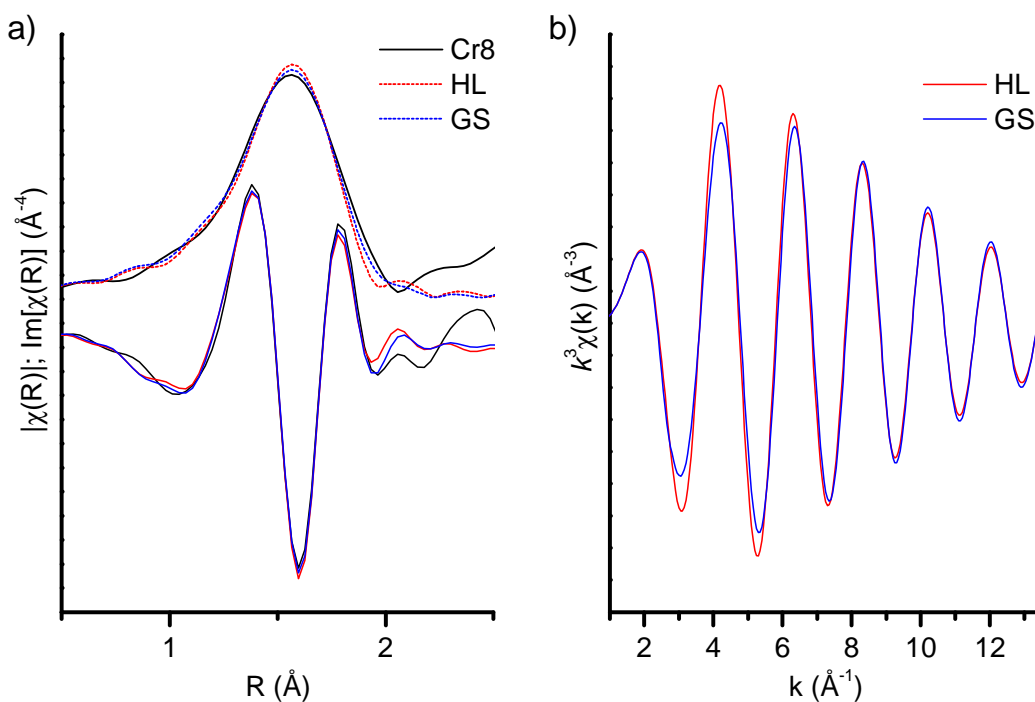


Figure S3: (a) Fourier transformed EXAFS of Cr8 and shell-fit result using theoretical Cr-O path calculated with the Hedin-Lundqvist (HL) and the ground state (GS) potential, respectively, for the atomic background. (b) EXAFS of the Cr-O single-scattering path simulated with FEFF with HL and GS potential for the atomic background. For both signals the same parameter set was used ($S02=1$, $E0=0 \text{ eV}$, $dR=0 \text{ \AA}$, $DWP_O=0.005 \text{ \AA}^2$).

Table S1: Results from EXAFS shell-fits of the first (Cr-O) shell (R-range: 1-2 Å) in Cr8 by using FEFF simulated path and amplitude functions calculated with the Hedin-Lundqvist (HL) potential and the ground state (GS) potential for the atomic background. Note: the fit parameters differ from the ones in Table 1, since the R-range differs and since no constraints were applied. Digits in parenthesis are estimated uncertainties.

Model	Atom	N	R (Å)	DWP (Å ²)	S ₀ ²	E ₀ (eV)	R (%)	χ _v ²
HL	O	6	1.99(1)	0.005(1)	0.77(13)	3(2)	1.00	736
GS	O	6	1.99(1)	0.006(1)	0.95(11)	2(2)	0.5	338

The choice of the exchange potential for the computation of the atomic background did not affect the trend observed in the shell-fitting results between Cr8 and Cr71. Using theoretical standards computed with the default settings (ixc0=0), the one-shell model (F1) gave the smallest χ_v² value in the case of Cr8, whereas for Cr71 the models F2 and F4 (including double-corner-sharing octahedra) gave the smallest χ_v² value (Table S2). These results were in full agreement with the results presented in Table 2. Still, for Cr71 the χ_v² of the two-shell model (F2) is only twice as small as the χ_v² of the one-shell model (Table S2). This decrease did not pass the significance test introduced in the main text. Thus, when using theoretical standards computed with the default settings the two-shell model can not be rated superior to the one-shell model based on the EXAFS analysis.

Table S2: Selected results from shell fits of Cr8 and Cr71 with the five fit models. In the FEFF calculation the Hedin-Lundqvist exchange potential was used for the atomic background. In the last column the χ_v^2 values are given relative to the ones of the corresponding fits using theoretical standards calculated with the ground state potential for the atomic background function (cf. Table 2). Fixed parameters for all fits: $E_0=1.5$ eV; $S_0^2=0.81$.

Sample	Mod.	N_1	N_2	N_3	$DWP_{1/2}$ (\AA^2)	DWP_3 (\AA^2)	N_{var}	R (%)	rel. R	χ_v^2	rel. χ_v^2	HL/GS
Cr8	<i>F1</i>	3.1	0	0	0.012	-	3	3.50	1.00	67	1.0	1.7
	<i>F2</i>	3.4	0	2	0.013	0.030	5	2.90	0.83	88	1.3	1.7
	<i>F3</i>	3.1	0	2 [§]	0.012	0.034	5	3.25	0.93	99	1.5	1.7
	<i>F4</i>	3.3	0.5	2	0.012	0.024	7	2.85	0.81	211	3.2	up [†]
	<i>F5</i>	2	up [†]	2 [§]	0.010	0.031	7	2.89	0.83	214	3.2	up [†]
Cr71	<i>F1</i>	1.5	0	0	0.008	-	3	7.66	1.00	235	1.0	1.2
	<i>F2</i>	1.4	0	2	0.007	0.017	5	2.97	0.39	145	0.6	2.6
	<i>F3</i>	1.5	0	2 [§]	0.007	0.020	5	6.20	0.81	302	1.3	1.2
	<i>F4</i>	3.0	1.8	2	0.011	0.015	7	1.73	0.23	206	0.9	4.8
	<i>F5</i>	2.6	1	2 [§]	0.010	0.021	7	3.28	0.43	391	1.7	1.9

[§]single corner-sharing distance (starting value: 4 \AA). [†]unphysical solutions (<0); fits with unphysical solutions were excluded from the comparison.

Notes: N_1, N_2, N_3 = degeneracies of the first ($R\sim 3$ \AA), second ($R\sim 3.3$ \AA) and third ($R\sim 3.5$ or 4 \AA) metal shell, respectively. N_{var} = the number of parameters varied during the fit. $DWP_1, DWP_2,$ and DWP_3 = DWP of the first, second, and third metal shell, respectively.

Cr and Fe as metal backscatterers

Table S3: Selected results from shell fits of Cr8 and Cr71 with the five fit models. For the FEFF calculation of the theoretical standards a goethite cluster was used in which all Fe were replaced by Cr atoms. In the last column the χ_v^2 values are given relative to the ones of the corresponding fits using theoretical standards calculated from a goethite cluster which contained only Fe atoms (except for the central Cr atom; cf. Table 2). Fixed parameters for all fits: $E_0=1.5$ eV; $S_0^2=0.95$.

Sample	Mod.	N_1	N_2	N_3	DWP _{1/2} (Å ²)	DWP ₃ (Å ²)	N_{var}	R (%)	rel. R	χ_v^2	rel. χ_v^2	Cr/Fe
Cr8	<i>F1</i>	2.6	0	0	0.012	-	3	2.73	1.00	52	1.0	1.3
	<i>F2</i>	2.9	0	2	0.013	0.027	5	1.69	0.62	51	1.0	1.0
	<i>F3</i>	2.7	0	2 [§]	0.012	0.033	5	2.44	0.89	74	1.4	1.2
	<i>F4</i>	2.3	0.7	2	0.011	0.022	7	1.57	0.58	117	2.2	up [†]
	<i>F5</i>	1.4	up [†]	2 [§]	0.008	up [†]	7	1.43	0.52	106	2.0	up [†]
Cr71	<i>F1</i>	1.4	0	0	0.007	-	3	4.94	1.00	152	1.0	0.8
	<i>F2</i>	1.2	0	2	0.006	0.019	5	1.52	0.31	74	0.5	1.3
	<i>F3</i>	1.4	0	2 [§]	0.007	0.022	5	3.90	0.79	191	1.3	0.7
	<i>F4</i>	2.5	1.4	2	0.010	0.017	7	0.45	0.09	53	0.4	1.2
	<i>F5</i>	2.1	0.6	2 [§]	0.009	0.022	7	1.72	0.35	205	1.4	1.0

[§]single corner-sharing distance (starting value: 4 Å). [†]unphysical solutions (<0); fits with unphysical solutions were excluded from the comparison.

Notes: N_1 , N_2 , N_3 = degeneracies of the first (R~3 Å), second (R~3.3 Å) and third (R~3.5 or 4 Å) metal shell, respectively. N_{var} = the number of parameters varied during the fit. DWP₁, DWP₂ and DWP₃ = DWP of the first, second and third metal shell, respectively.

Appendix 3. Fourier transformed EXAFS

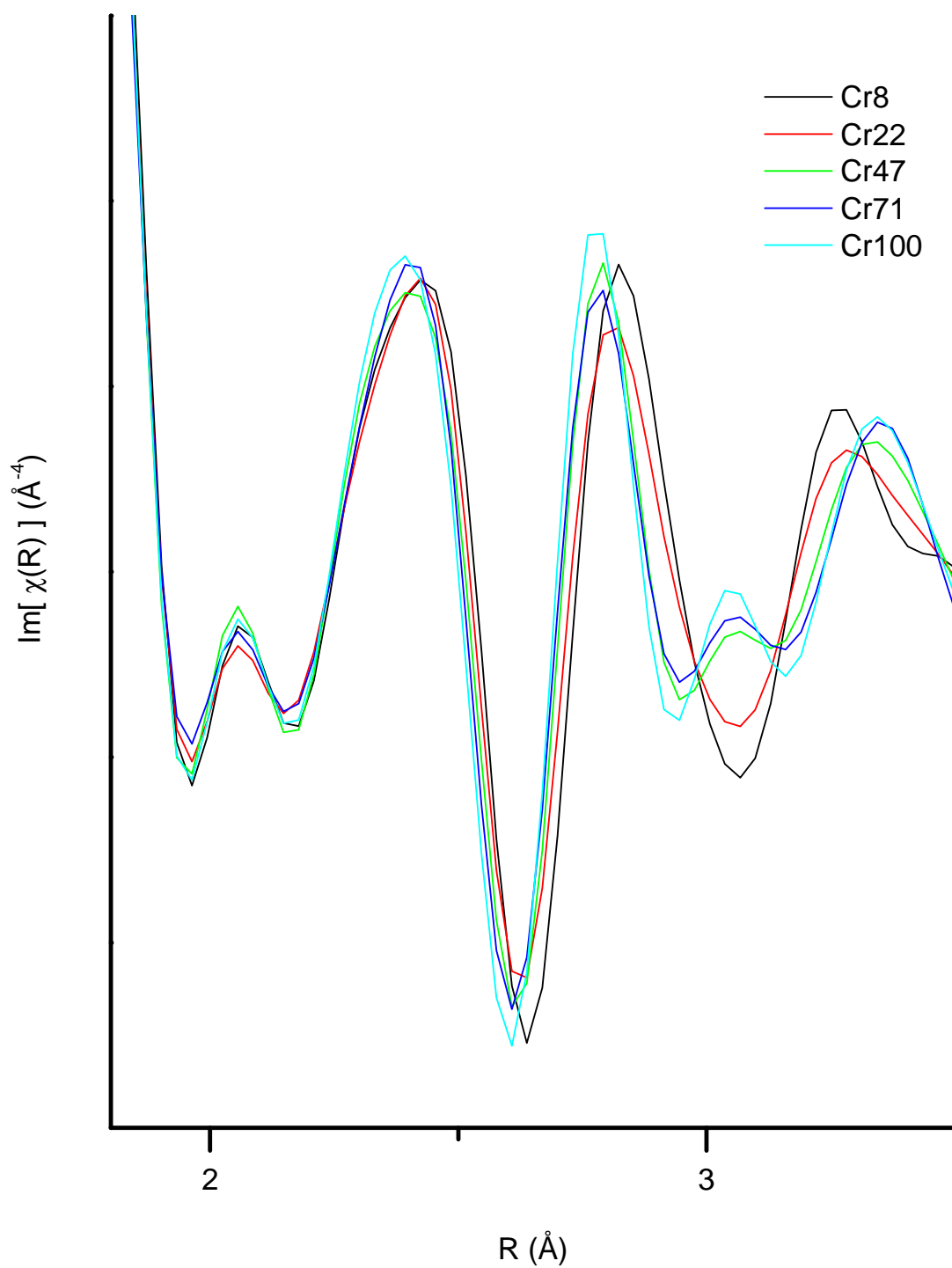


Figure S4: Magnified view of the imaginary part of the Fourier transformed Fe-Cr-oxyhydroxide EXAFS spectra.

Appendix 4. High-energy-resolution spectra

From selected samples we collected high-energy-resolution fluorescence-detected (HERFD) XANES spectra, in which the deep core state lifetime broadening is effectively suppressed. In these spectra individual XANES features are highlighted and the determination of their energy position is facilitated. For the purpose of our study the HERFD data are required to confirm the number and energy position of the features in the negative second derivative spectra of the conventional XANES spectra. This is particularly useful for cases in which the detection of peaks in the negative second derivative spectra of the conventional spectra is not unambiguous. Figure S5 shows the HERFD XANES spectra of the two crystalline reference compounds and of Cr8 and Cr71, along with the corresponding negative second derivative spectra. Fluorescence-detected XAS spectra of samples highly concentrated in the analyte may be affected by the over-absorption effect (Manceau et al., 2002). Qualitative comparisons with the conventional (transmission) spectra suggested that this effect was small for the grimaldiite sample, while it was much stronger for Cr71. Because of the large correction required for Cr71, the peak intensities in the corrected Cr71 spectrum may still be affected by the over-absorption effect (the effect on the peak positions is expected to be negligible). The negative second derivatives of HERFD XANES spectra of the two crystalline oxyhydroxides (Figure S5) were overall in close agreement with the ones of the conventional spectra. The features in the whitenline regions of the two weakly crystalline samples, i.e., Cr8 and Cr71, on the other hand, were much better resolved in the negative second derivative spectra of the HERFD XANES data. For Cr8 the existence of a smaller peak at 6004 eV and a more intense one at 6008.8 eV was confirmed. For Cr71 the negative second derivative of the HERFD XANES spectrum clearly confirmed the existence of a second peak at about 6010 eV, besides the more intense one at 6006 eV. The second peak was not fully resolved in the negative second derivative of the conventional spectrum (Figure 4).

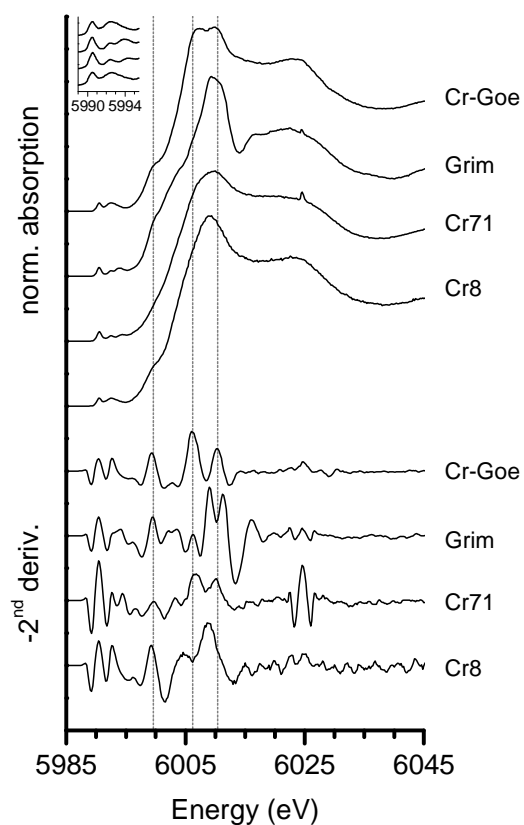


Figure S5: HERFD XANES spectra of Cr-Goe, Grim, Cr8, and Cr71 along with the corresponding negative second derivative spectra. The negative second derivative spectra of Cr-Goe and Grim are multiplied by 2, whereas the ones of Cr8 and Cr71 are multiplied by 4. The inset shows a zoom into the pre-edge region.

Appendix 5. Additional XANES simulation

To approximate the spectrum of a Cr octahedron surrounded by more than two edge-sharing octahedra at the same metal-metal distance we did a FEFF-simulation by using the SCF-potentials calculated for the Cr-goethite cluster and atomic input coordinates derived from the crystal structure of grimaldiite (in which the Cr octahedra share edges with six neighboring Cr octahedra). This simulation is only an approximation, since the potentials were calculated for a different cluster and because the Cr-O distances within the CrO₆-octahedra in the crystallographic data of grimaldiite (Christensen et al., 1977) are fully coherent (i.e., no structural disorder), which does likely not reflect the real situation (cf. EXAFS results). Despite these limitations the XANES spectra simulated by using a 6.5 Å-radius-cluster reproduced the main-characteristics of the experimental spectrum of grimaldiite except for the small split in the whitenline at about 6010 eV (data not shown). However, the spectra needed to be shifted by -1 eV relative to the simulated Cr-goethite spectra.

Figure S6 shows that successively including more edge-sharing octahedra resulted in an increased intensity of the peak at 6008 eV and of the shoulder at 6000 eV. The difference between spectrum s2 and s3 showed that the simulated spectra are not only influenced by the number of the octahedra, but also by the symmetry of the cluster; despite a slight shift in the energy position of the peak at 6009 eV in spectrum s2 compared to s3, the main pattern (broad shoulder at 6004 eV and an intense peak at about 6009 eV) is obtained for both clusters.

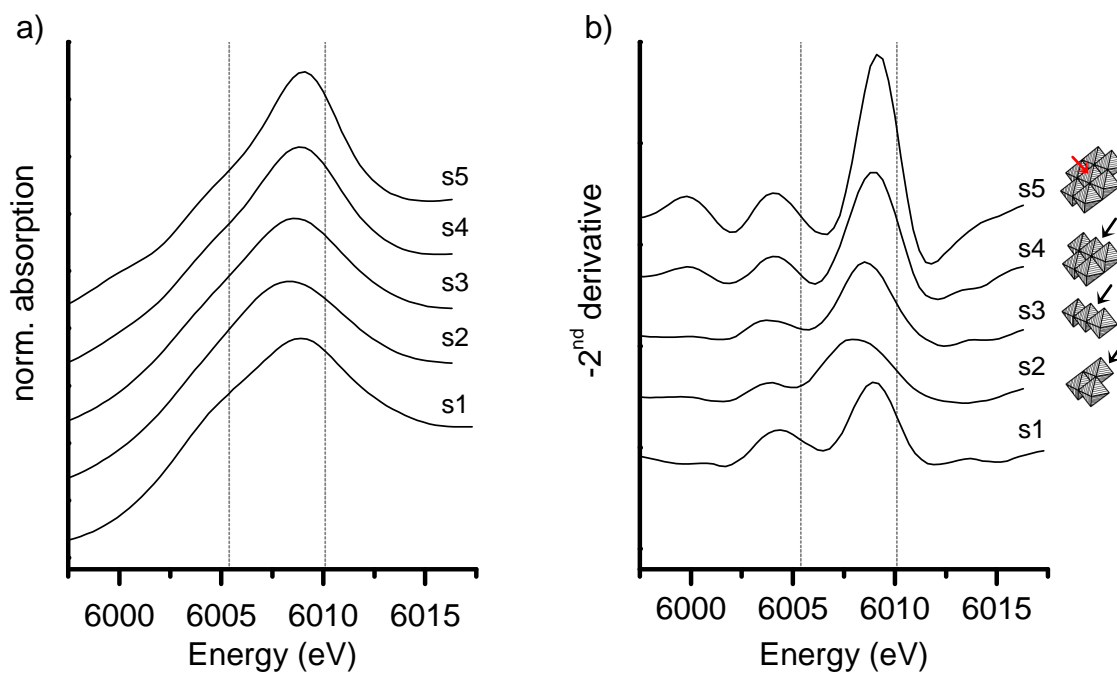


Figure S6: FEFF simulated XANES spectra for different clusters derived from the crystal structure of grimaldiite (using the SCF-potentials calculated for Cr-goethite). The simulated spectrum (a) and the corresponding negative second derivate spectra are shown (b). The clusters used for the calculation are shown on the right; small arrows indicate the position of the octahedron with the absorber Cr atom. Spectrum s1: edge-sharing cluster from the Cr-goethite structure (cf. s1 in Figure 5) for comparison (the structure is similar to s3). The theoretical spectra obtained from the grimaldiite cluster are shifted by -1 eV relative to the spectra obtained from Cr-goethite.

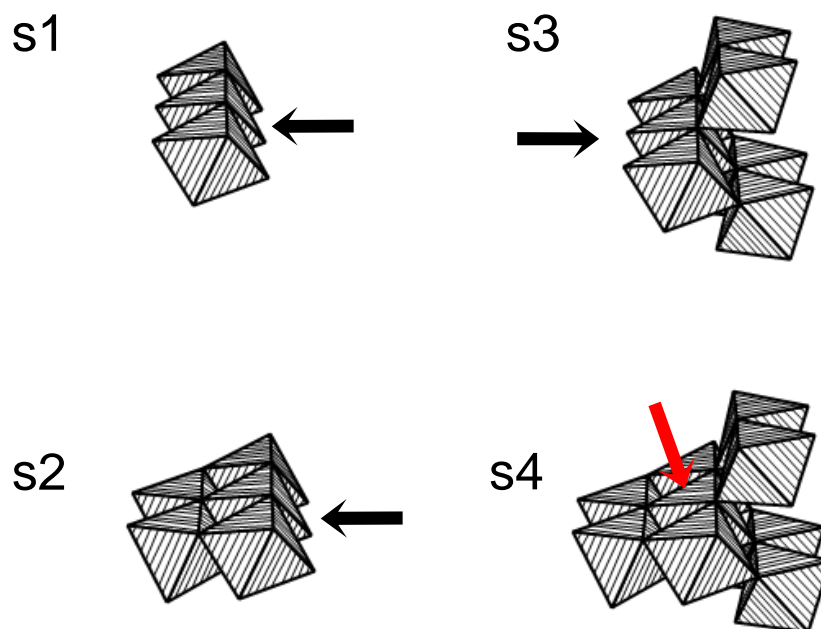


Figure S7: Enlarged view of the clusters used for the simulation of the XANES spectra shown in Figure 5. Arrows indicate the position of the central octahedron containing the Cr absorber atom in simulations s1-s4.

Appendix 6. Second derivative spectra

Taking the negative second derivative of a signal is a powerful tool for determining the number and position of the peaks in this signal. Figure S8 shows the first and second derivatives of a Gaussian. The negative second derivative contains negative side lobes. If the side lobes of two peaks overlap, they may form a spurious secondary maximum (which has no counterpart in the original signal). If two peaks of equal intensity are located very close to each other, interferences involving the side lobe may cause a shift in the intensity and the position of the peaks in the negative second derivative (Figure S9).

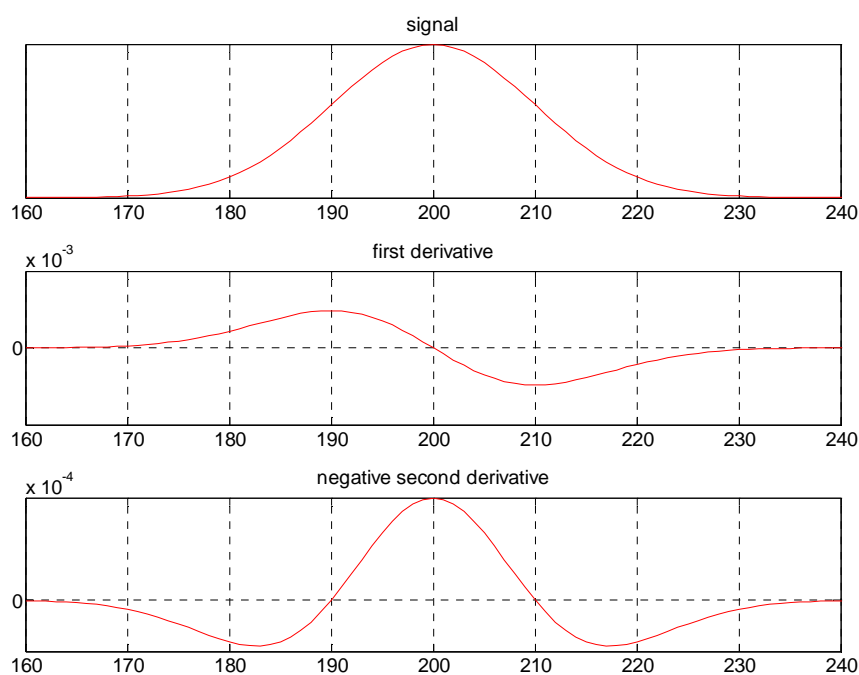


Figure S8: Gaussian, its first derivative and its second derivative. Arbitrary units were used for both axes.

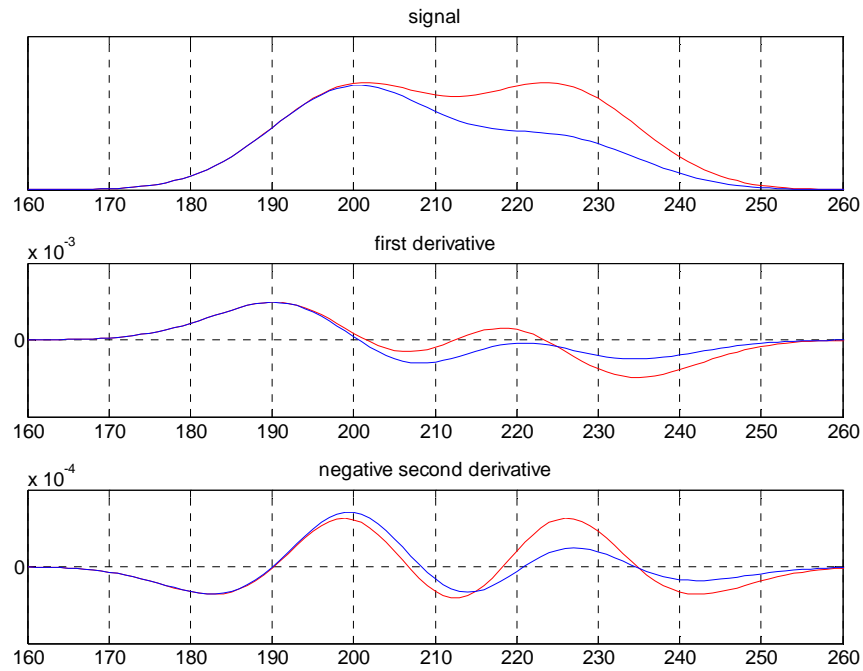


Figure S9: Sum of two Gaussians located close to each other (located at 200 and 225, respectively). Two cases are considered: two Gaussians of equal height (red) and the height of the second Gaussian is half as high as the height of the first (blue). The sum signal, the first and the negative second derivatives are shown. Arbitrary units were used for both axes.

References cited

- Boyanov, M.I., Kemner, K.M., Shibata, T., and Bunker, B.A. (2004) Local structure around Cr³⁺ ions in dilute acetate and perchlorate aqueous solutions. *Journal of Physical Chemistry A*, 108(23), 5131-5138.
- Christensen, A.N., Hansen, P., and Lehmann, M.S. (1977) Isotope effects in the bonds of α -CrOOH and α -CrOOD. *Journal of Solid State Chemistry*, 21(4), 325-329.
- Hudson, E.A., Allen, P.G., Terminello, L.J., Denecke, M.A., and Reich, T. (1996) Polarized X-ray-absorption spectroscopy of the uranyl ion: Comparison of experiment and theory. *Physical Review B (Condensed Matter)*, 54(1), 156-165.
- Manceau, A., M.A. Marcus, N. Tamura (2002) Quantitative speciation of heavy metals in soils and sediments by synchrotron X-ray techniques. In R.M.L. Fenter P.A., Sturchio N.C., Sutton S.R., Ed. *Applications of synchrotron radiation in low-temperature geochemistry and environmental sciences*, 49, p. 341-428. Mineralogical Society of America
- Voegelin, A., Kaegi, R., Frommer, J., Vantelon, D., and Hug, S.J. (2010) Effect of phosphate, silicate, and Ca on Fe(III)-precipitates formed in aerated Fe(II)- and As(III)-containing water studied by X-ray absorption spectroscopy. *Geochimica et Cosmochimica Acta*, 74, 164-186.